Journal of Materials Chemistry A

ROYAL SOCIETY OF CHEMISTRY

PAPER

View Article Online
View Journal | View Issue

Cite this: J. Mater. Chem. A, 2026, 14, 15085

NiFe alloy nanocrystals anchored on nitrogen-doped carbon: interface engineering for enhanced peroxymonosulfate activation *via* non-radical dominated pathways

Xiaoqin Sun,*[a] Meiluo Jiang,[a] Hao Chen,[a] Hongmei Chen[e] and Xiaoxiang Xu *[bcd]

Peroxymonosulfate (PMS) activation based on non-radical oxidation has emerged as a highly efficient and feasible strategy for wastewater treatment. Herein, heterogeneous catalysts with NiFe alloy nanocrystals anchored on nitrogen-doped carbon (NiFe–N-C) were rationally designed and fabricated to activate PMS for the degradation of tetracycline (TC). The NiFe–N-C/PMS catalytic system achieved 93.3% TC removal and 79.8% PMS utilization within 60 minutes, outperforming analogous catalytic systems previously reported. Notably, the system exhibited strong anti-interference against various anions and humic acid (HA) and maintained high catalytic activity over a broad pH range, highlighting its strong adaptability to complex practical water environments. Singlet oxygen ($^1O_2$) and high-valent metal species (HVMSs) were identified as the dominant oxidants for TC degradation. DFT calculations further revealed that the Ni/Fe dual active sites served as the dominant catalytic centers in NiFe–N-C, which could reduce the energy barrier for O–O bond cleavage of PMS, thereby facilitating the formation of $NiFe^{IV}$=O species and $^1O_2$. Additionally, the N-C matrix stabilizes NiFe alloy nanocrystals through the formation of strong surface N–M bonds, while enabling rapid interfacial electron transfer in the catalytic system. Finally, comprehensive analyses of degradation pathways and toxicity evaluations confirmed the environmental safety of the catalytic process. This study provides a theoretical basis for high-performance non-radical catalytic system design and lays a foundation for their practical application in water pollution control.

Received 29th December 2025
Accepted 24th February 2026

DOI: 10.1039/d5ta10557a

rsc.li/materials-a

1. Introduction

Antibiotic wastewater discharge poses a significant threat to environmental safety and human health. Tetracycline (TC), a typical broad-spectrum antibiotic, is widely used to treat bacterial infections in humans and animals due to its low cost and high efficacy.[1] However, TC features complex molecular structures and high chemical recalcitrance, which render conventional water treatment methods ineffective, often leading to incomplete degradation and persistent residual contamination in aquatic environments.[2] Consequently, the development of eco-friendly and efficient methods for its removal is of paramount importance.

Advanced oxidation processes (AOPs) based on peroxymonosulfate (PMS) activation have attracted extensive attention due to their strong oxidation capacity, wide pH adaptation range, and long-lasting reactive oxygen species (ROS) generation.[3] PMS can be activated using various catalysts to generate multiple reactive species with high oxidation potentials, such as sulfate radicals ($SO_4^{\cdot-}$), hydroxyl radicals ($\cdot OH$), and singlet oxygen ($^1O_2$), which can effectively degrade most organic pollutants.[4,5] Nevertheless, the efficiency of PMS activation is highly dependent on the performance of the catalyst. The design and preparation of catalysts with high activation efficiency, excellent stability, and low cost is the core of this technology.

Transition metal-based catalysts, with unique d-orbital electron configurations and redox activity, are widely used in PMS activation.[6] For example, Li *et al.* prepared a three-dimensional hollow tubular surface-loaded cobalt/cotton carbon fiber composite (Co–CCF-600) by carbonizing cotton. This composite catalyst could effectively activate PMS to degrade carbamazepine (CBZ) with 93.47% efficiency in 60

[a]School of Chemistry and Chemical Engineering, Xi'an University of Architecture and Technology, Xi'an 710055, Shaanxi, China. E-mail: sunxiaoqin@xauat.edu.cn
[b]Department of Neurosurgery, Tongji Hospital, Tongji University School of Medicine, Tongji University, Shanghai, 200065, P. R. China. E-mail: xxxu@tongji.edu.cn
[c]Clinical and Central Lab, Putuo People's Hospital, Tongji University, Shanghai, 200060, P. R. China
[d]Shanghai Key Lab of Chemical Assessment and Sustainability, School of Chemical Science and Engineering, Tongji University, Shanghai, China
[e]Wenzhou Key Laboratory of Novel Optoelectronic and Nanomaterials, Institute of Wenzhou, Zhejiang University, 26 Fengnan Road, Wenzhou 325006, China

minutes.[2] Zhao *et al.* synthesized a tungsten iron phosphate boride composite ($FePO_4$/WB), which achieved efficient degradation of neonicotinoid insecticides (NEOs) in PMS-activated systems relying on rapid Fe(III)/Fe(II) redox cycles.[7] Jin *et al.* developed a pyrolysis-free strategy to construct transition metal single-atom catalysts (SAC_{4+1}) with well-defined axial FeN coordination structures, significantly enhancing PMS activation ability.[8] However, single transition metal systems often suffer from inherent drawbacks, including nanoparticle agglomeration, unstable surfaces, and poor electron transfer, which would reduce catalytic durability and anti-interference ability.[9]

To address these limitations, two effective strategies have been proposed. One is the fabrication of bimetallic composites that leverage synergistic catalytic mechanisms to enhance performance.[10,11] For instance, Zhu *et al.* designed a catalyst by anchoring diatomic $FeCoN_6$ on porous carbon carriers. The composite exhibited higher conversion frequencies than single FeN_4 or CoN_4 systems and achieved excellent degradation of sulfamethoxazole.[12] Li *et al.* developed an Fe/Mn co-loaded hydroxyl-rich biochar composite (FeMn–OH–BC) for PMS activation, which not only achieved over 85% TC removal across a wide pH range (5–9) but also showed remarkable anti-interference capacity, with anion-induced inhibition kept below 15%.[11] The other is the use of carbon materials as supports for transition metal-based catalysts, attributed to their superior electron-donating capabilities and structural stability.[13] Carbon materials, such as graphene, carbon nanotubes, and porous carbon, have large specific surface areas, good electrical conductivity, and high chemical stability. These intrinsic properties enable them to serve as ideal supports for transition metal nanoparticles, effectively mitigating nanoparticle agglomeration while synergistically boosting catalytic activity *via* strong metal–carbon interactions.[14] The introduction of nitrogen atoms into carbon materials (N-C) can further adjust their electronic structure, increase the number of active sites, and improve the adsorption capacity of pollutants and PMS, thereby promoting the catalytic reaction.[15] Xiao *et al.* developed nitrogen-doped carbon nanotube-encapsulated iron nanoparticle catalysts (Fe/Fe_3C@NCNTs) for efficient activation of PMS and TC degradation. The encapsulated structure greatly reduces the leaching of metal ions, and the presence of nitrogen-doped nanotubes allows graphitic nitrogen to act as a catalytic center to promote Fe^{II}/Fe^{III} cycles and ROS generation.[16] Hu *et al.* synthesized a Ni/Co LDH@NC catalyst using ZIF-67 as a template, which achieved complete removal of sulfamethoxazole (SMX) within 60 minutes and maintained high performance after multiple cycles.[17] Given the complementary advantages of bimetallic composites and N-C supports, the integration of bimetallic nanoparticles and N-C supports is expected to yield high-efficiency PMS activation catalysts, overcoming the limitations of single-metal and common carbon catalysts. However, the traditional synthesis strategies for N-C skeletons suffer from intricate procedures and poor controllability over structural parameters.[18,19] Moreover, the underlying synergistic activation mechanism of PMS, including the electron transfer pathway between bimetallic components, the role of N-C in modulating catalytic activity, and the dynamic interaction between metals and carbon supports, remains unclear and necessitates detailed exploration.

Herein, NiFe alloy nanocrystals anchored on nitrogen-doped carbon (NiFe–N-C) catalysts were successfully prepared by high-temperature pyrolysis of polyaniline (PANI). The NiFe–N-C catalyst exhibited excellent performance in activating PMS for TC degradation, achieving a high removal efficiency of 93.3%. Moreover, it possessed strong anti-interference ability against common anions and excellent applicability over a wide pH range. Notably, the N-C matrix stabilized the NiFe alloy nanocrystals, endowing the catalyst with good stability and reusability. Furthermore, this study revealed the regulatory role of NiFe loading in modulating the dominant reactive species during PMS activation. Previous reports demonstrated that pristine N-C mainly followed a hydroxyl radical-dominated process,[20] whereas NiFe–N-C redirected the PMS activation mechanism toward a non-radical pathway governed by high-valent metal species (HVMSs) together with $^1O_2$. DFT calculations further confirmed that NiFe incorporation significantly lowered the energy barrier for HVMS formation and rendered $^1O_2$ generation exothermic, thereby synergistically boosting the catalytic efficiency. Finally, the intermediate products generated during TC degradation were analyzed, and possible degradation pathways were deduced. This study aims to provide new insights into the design and preparation of high-efficiency catalysts dedicated to the removal of antibiotic pollutants in water.

2. Experimental

2.1 Chemicals and materials

All chemicals are analytically pure grade and can be used directly without any purification. Details regarding chemicals and materials are provided in Text S1 of the SI.

2.2 Synthetic procedures

The synthesizing procedure of NiFe–N-C is briefly displayed in Fig. 1a. Initially, 0.1 g of PANI was dispersed in 20 mL of anhydrous ethanol to achieve homogeneity. Subsequently, 0.05 g of $Fe(NO_3)_3\cdot 9H_2O$ and 0.05 g of $Ni(NO_3)_2\cdot 6H_2O$ were added to the solution and stirred for 24 h at ambient temperature. The mixture was then dried in a drying oven at 60 °C for 12 h to obtain powdered NiFe PANI. The NiFe PANI was then placed in a tube furnace and heated to 800 °C with an increasing rate of 5 °C min^{-1} under a nitrogen atmosphere for a duration of 2 h.

Characterization (Text S2), experimental procedures (Text S3), and analytical methods (Text S4) are presented in the SI.

3. Results and discussion

3.1 Characterization

The morphologies of PANI, N-C and NiFe–N-C catalysts were characterized by SEM. Pristine PANI comprises interwoven nanofibers forming a regular mesh structure (Fig. S1), endowing it with high porosity.[21] In contrast, the N-C derived from high-

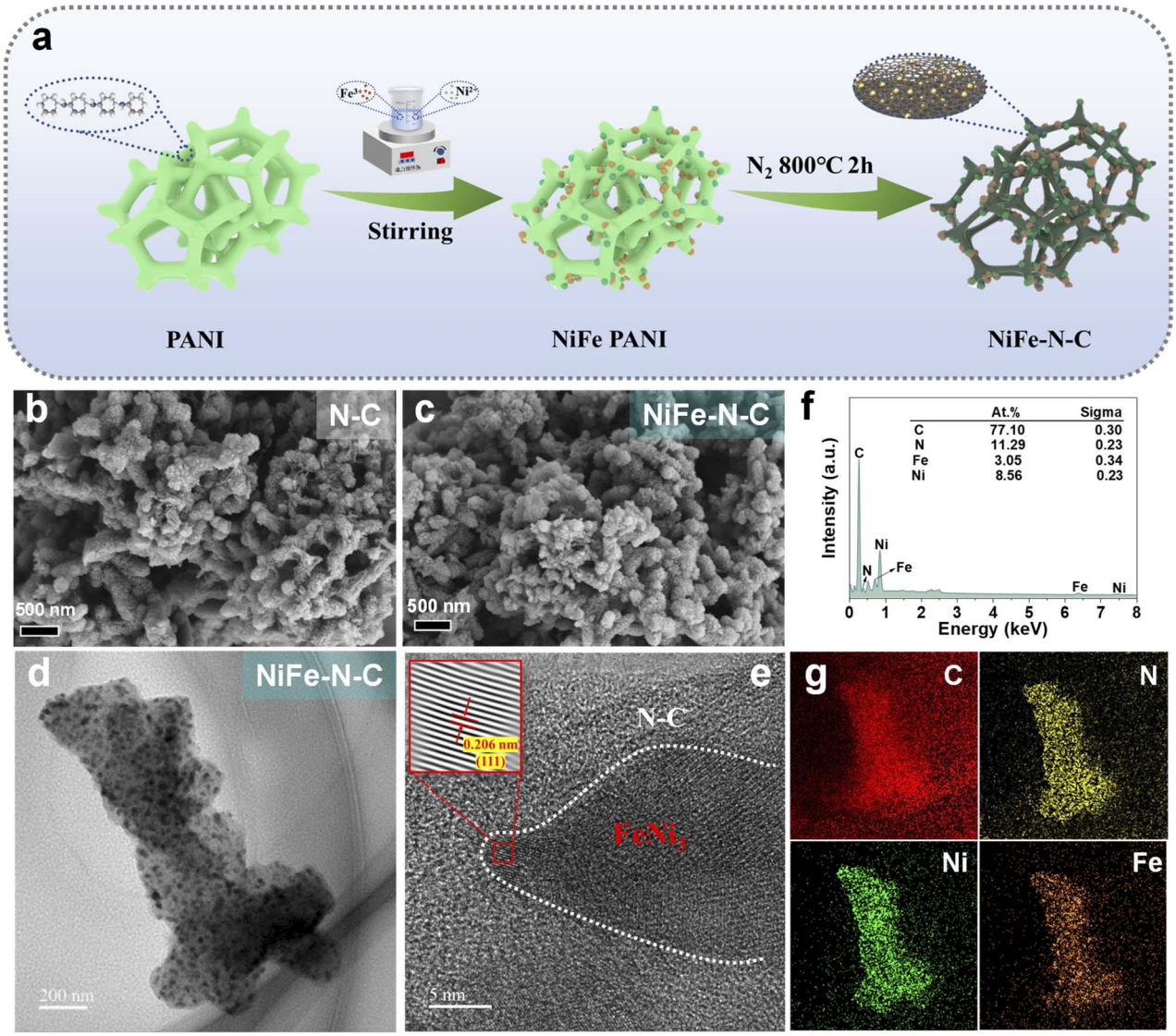

Fig. 1 (a) Schematic diagram of the preparation of NiFe–N-C; SEM images of (b) N-C and (c) NiFe–N-C; (d) TEM image of NiFe–N-C; (e) HRTEM image of NiFe–N-C; (f) EDS and (g) elemental mapping of NiFe–N-C.

temperature pyrolysis exhibits enlarged dimensions but retains the favourable skeletal structure of PANI (Fig. 1b). The morphology of NiFe–N-C was comparable to that of N-C (Fig. 1c), suggesting that the incorporation of NiFe did not alter the original skeletal morphologies. Moreover, the fine morphologies of NiFe–N-C were investigated by TEM. As shown in Fig. 1d, NiFe nanoparticles are uniformly anchored on the surface of N-C nanofibers. The high-resolution TEM (HRTEM) image (Fig. 1e) reveals a lattice spacing of 0.206 nm, corresponding to the (111) crystal planes of the $FeNi_3$ alloy. Meanwhile, discontinuous lattice fringes in the surrounding region indicate graphitization. Moreover, a sharp and distinct interface was clearly visible between $FeNi_3$ nanocrystals and the N-C matrix, which confirmed intimate contact between the two components. In addition, EDS analysis verifies the coexistence of Ni, Fe, N, and C elements in the NiFe–N-C catalyst and the molar ratio of Ni/Fe is close to 3 : 1 (Fig. 1f, inset table). Furthermore, thermogravimetric analysis (TGA, Fig. S2) reveals that the mass content of the C–N matrix is 15.26%. Elemental mapping results demonstrate the uniform distribution of C, N, Ni and Fe across NiFe–N-C (Fig. 1g), which further confirms the homogeneous immobilization of NiFe nanocrystals on the N-C matrix.

The crystal structures of the as-prepared catalysts were analyzed by XRD (Fig. 2a). For the N-C catalyst, two broad diffraction peaks appeared at 23.8° and 44.2°, which are assigned to the (002) and (100) lattice planes of graphitic carbon, respectively.[22] Notably, the NiFe–N-C catalyst exhibited a distinct broad peak centered at 22.5°, confirming the retention of graphitized carbon in the composition. The peak shift relative to N-C is presumably attributed to the interaction between Ni/Fe and nitrogen species in the carbon matrix,[23] which induces structural distortions and modulates the intrinsic electronic properties of the graphitized carbon matrix.

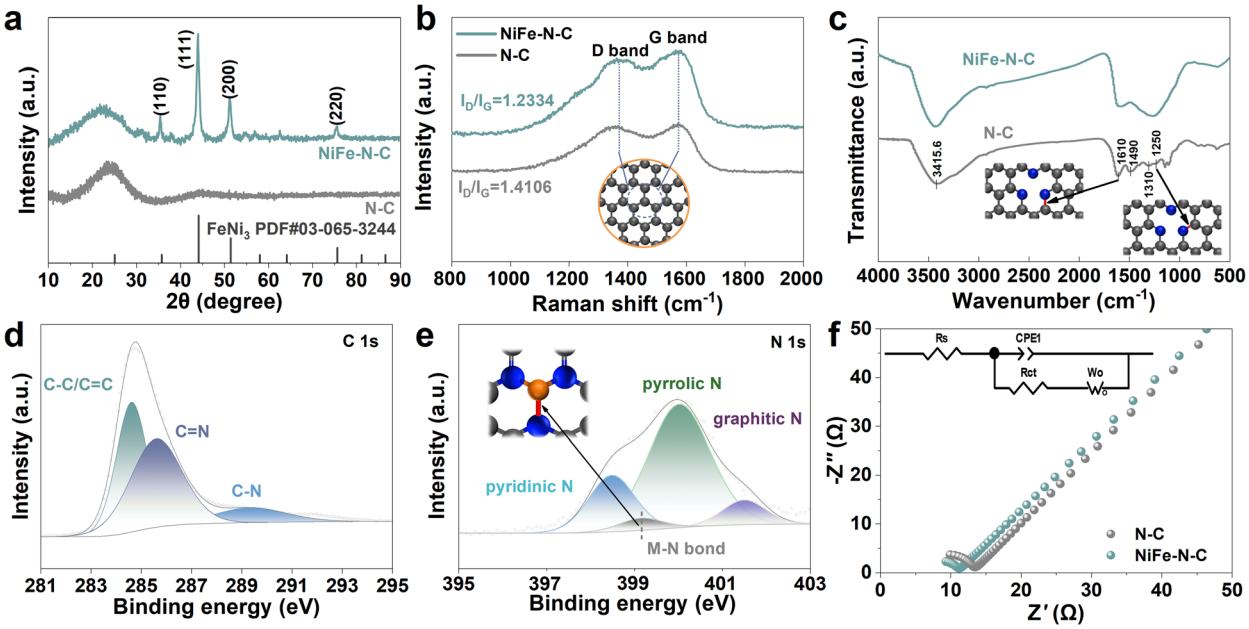

Fig. 2 (a) XRD patterns; (b) Raman spectra; (c) FT-IR spectra; (d) C 1s and (e) N 1s XPS spectra in NiFe–N-C; (f) Nyquist plot.

Furthermore, the NiFe–N-C catalyst displays characteristic diffraction peaks at 35.5°, 44.1°, 51.4° and 75.7°, corresponding to the (110), (111), (200) and (220) crystal planes of the $FeNi_3$ phase (PDF #03-065-3244), which verify the successful formation of the bimetallic phase in the composite. Raman spectroscopy was subsequently utilized to characterize the structural features of N-C within the catalysts (Fig. 2b). Both N-C and NiFe–N-C displays distinct characteristic peaks at approximately 1350 cm^{-1} and 1580 cm^{-1}, assigned to the D and G bands of the carbon material, respectively.[24] Notably, NiFe–N-C shows a smaller I_D/I_G ratio compared to pristine N-C. This result indicates that the introduction of NiFe reduces the defect density in the carbon framework of the catalysts, which in turn endows them with a more ordered structure.[25] To further clarify the surface functional groups of the catalysts, FT-IR was conducted. As shown in Fig. 2c, all samples display a broad absorption band around 3415.6 cm^{-1}, which is consistent with the O–H stretching vibration from surface hydroxyl groups.[26] Moreover, the peaks located at 1490 cm^{-1} and 1310 cm^{-1} are assigned to the ring stretching vibrations of graphitic carbon, while the absorption peaks around 1250 cm^{-1} and 1610 cm^{-1} are attributed to the stretching vibrations of C–N and C=N, respectively.[27] Additionally, the high-resolution XPS C 1s spectrum can be deconvoluted into three characteristic peaks at 284.8, 285.6 and 289.4 (Fig. 2d), which are assigned to C–C/C=C, C=N and C–N species, respectively. Likewise, the N 1s spectrum exhibits distinct peaks at 398.7 eV, 400.1 eV and 401.3 eV, which correspond to pyridine nitrogen, pyrrole nitrogen and graphite nitrogen, respectively (Fig. 2e),[28] further confirming the successful incorporation of N into the carbon matrix. More importantly, a well-defined peak at 399.2 eV is assigned to metal–nitrogen (M–N) bonds (Fig. 2e),[28] providing direct evidence for the formation of robust chemical interactions between the N-C matrix and NiFe nanocrystals. The N_2 adsorption–desorption isotherms also reveal that NiFe–N-C has a larger BET surface area than the pristine N-C counterpart (Fig. S3). Such an enhanced surface area is conducive to providing abundant active sites, thereby facilitating the adsorption of reactants during the catalytic process. Electrochemical impedance spectroscopy (EIS) was employed to evaluate the electron transfer behavior at the catalyst interface. The Nyquist plots of the catalysts exhibit high-frequency semicircular arcs and low-frequency linear regions (Fig. 2f), which correspond to the interfacial charge-transfer resistance (R_{ct}) and the solution diffusion process, respectively. As derived from the simulated equivalent circuit (Fig. 2f, insert), the NiFe–N-C composite possesses a notably smaller R_{ct} value (4.77 Ω) than the pristine N-C counterpart (7.23 Ω), demonstrating accelerated interfacial charge transfer kinetics.[29] Thus, these superior physicochemical and electrochemical properties enable NiFe–N-C to effectively promote the kinetics of the target catalytic reaction.

3.2 Catalytic performance of the NiFe–N-C catalyst

The PMS activation performance of the synthesized catalysts was evaluated *via* a series of comparative experiments focused on TC removal. As shown in Fig. 3a, the pristine N-C catalyst achieved a TC degradation efficiency of 73.0% within 60 minutes. This performance can be primarily attributed to its abundant surface functional groups, which serve as electron transfer mediators to trigger PMS activation.[30] In contrast, the single metal modified counterparts (Ni–N-C and Fe–N-C) exhibited either comparable or slightly reduced TC degradation efficiency relative to N-C, which can be ascribed to the inadequate interfacial electron transfer between the monometallic components (Ni or Fe) and the N-C matrix.[31] In

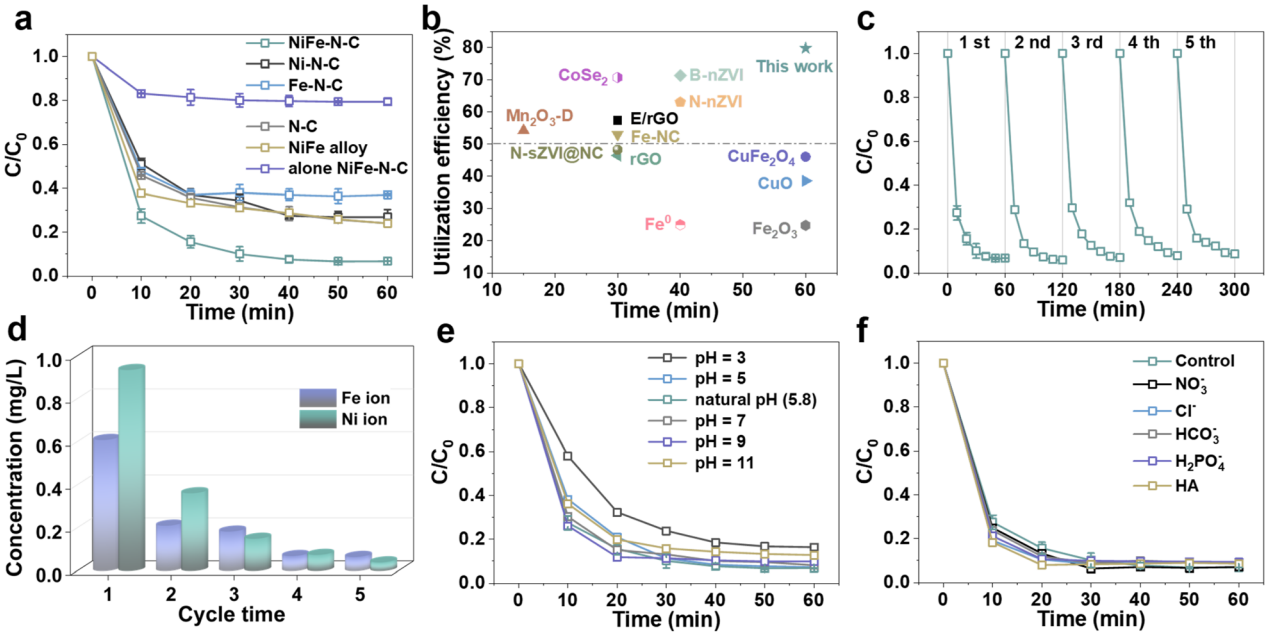

Fig. 3 (a) TC degradation in PMS activation with different catalysts; (b) comparison of UE_{PMS} in different catalytic systems; (c) successive cyclic runs of TC degradation in the NiFe–N-C/PMS system; (d) leaching concentrations of Fe and Ni ions during successive cyclic runs; (e) effect of initial pH on TC degradation; and (f) effect of the co-existence of inorganic anions and humic acid on TC degradation in the NiFe–N-C/PMS system. Reaction conditions: $m_{catalyst} = 20$ mg, $[TC]_0 = 10$ mg L^{-1}, [oxidant] = 1 mM, natural pH and $T = 298$ K.

addition, the bare NiFe alloy exhibited a TC removal efficiency of 76.1%. Notably, the introduction of NiFe bimetals into the N-C matrix significantly boosted the catalytic activity, where the NiFe–N-C composite achieved a TC degradation efficiency of 93.3% within the same reaction period, demonstrating the synergistic effect between the bimetallic components and the N-C support. To eliminate the interference of adsorption with the pollutant removal efficiency, control adsorption experiments were performed under the same conditions but without the addition of PMS (NiFe–N-C alone). The results indicate that the NiFe–N-C composite exhibits a low TC adsorption efficiency of 20.5%. Thus, these findings strongly indicate that the efficient removal of TC in our system is predominantly attributable to the enhanced activation of PMS by the NiFe–N-C/PMS catalytic systems. Meanwhile, the mineralization efficiency of the system was evaluated by Total Organic Carbon (TOC) analysis. The result showed that the TOC removal efficiency reached 56.1% after 120 min of reaction (Fig. S4), confirming that the system possessed strong deep oxidation performance rather than only partial bond cleavage of TC.

Subsequently, NiFe–N-C was employed to activate various oxidants as shown in Fig. S5. The catalyst displays distinct activation performance toward different oxidants, but none are comparable to that of activating PMS. This is attributed to the asymmetric structure of PMS, which renders it more susceptible to catalytic decomposition.[32] Further assessment of PMS utilization was achieved *via* control experiments. As illustrated in Fig. S6, negligible PMS self-decomposition occurred in the absence of a catalyst, whereas NiFe–N-C introduction dramatically accelerated PMS decomposition kinetics, confirming its prominent PMS activation capability. The PMS utilization efficiency (UE_{PMS}) reaches 79.8%, which not only outperforms the values reported in previous analogous studies (Fig. 3b and Table S1), but also exceeds the theoretical limit of the radical pathway. This implies that non-radical active species may act as the dominant active substances in this catalytic system.[33]

Additionally, the stability and reproducibility of the NiFe–N-C/PMS catalytic system were evaluated *via* consecutive cycle experiments (Fig. 3c). The results showed that the TC degradation efficiency remained at 91.3% of its original level after five cycles, demonstrating excellent recyclability. During the degradation process, the solution pH rapidly decreased and then remained stable (Fig. S7). This change can be attributed to the generation of acidic species and intermediates during the PMS activation and TC degradation.[34] More importantly, ICP measurements confirmed that the leaching concentrations of Fe and Ni ions were consistently below 1 mg L^{-1} in each cycle (Fig. 3d), confirming the stabilizing effect of N-C on NiFe alloys in accordance with XPS analysis. Furthermore, XRD (Fig. S8) and TEM (Fig. S9) characterization demonstrated that the catalyst maintained excellent structural integrity after the reaction. These results verified the outstanding reusability and environmental benignity of the catalytic system.

The catalytic performance of NiFe–N-C is closely related to the loading of the N-C matrix.[35] Thus, NiFe–N-C catalysts were synthesized with varying PANI addition amounts (50 mg, 100 mg, and 200 mg) to modulate the N-C content, and their performance in activating PMS for TC removal was evaluated (Fig. S10). It is evident that the catalytic system achieves the optimal TC removal efficiency when 100 mg of PANI is added.

Specifically, a low PANI dosage leads to the formation of N-C with insufficient capacity to support the dispersion of metals, resulting in metal agglomeration at the catalyst surface.[36] Conversely, an excessive PANI dosage results in a relatively low metal content, which is insufficient to generate an adequate number of active sites.[37]

To identify the optimal operating parameters for the NiFe–N-C/PMS system, we first investigated the effect of catalyst dosage on TC degradation efficiency (Fig. S11). The results indicate that the TC degradation efficiency first increases and then decreases with increasing catalyst dosage. In the low dosage range (<20 mg), a higher catalyst loading provides more abundant catalytically active sites, which enhances the activation efficiency of PMS and thus promotes TC degradation. However, excessive catalyst dosage induces particle agglomeration, leading to the coverage of partial active sites and a consequent decline in degradation efficiency.[38] On the other hand, PMS concentration was found to exert a significant impact (Fig. S12). When the PMS concentration increases from 0.5 mM to 1 mM, the TC degradation efficiency is remarkably enhanced. This is because the active sites in the catalytic system are not fully utilized at lower PMS concentrations.[39] With an appropriate increase in PMS dosage, more PMS is activated to generate reactive species, thereby boosting the degradation effect. However, a further increase in PMS concentration (>1 mM) leads to a decreasing trend in degradation efficiency. This phenomenon is mainly attributed to the self-quenching effect induced by excess PMS as shown in eqn (1) and (2), resulting in the depletion of ROS and a consequent reduction in the effective reactive activity of the system.[40] Finally, the effect of initial TC concentration was evaluated (Fig. S13). It was observed that the initial concentration affects the TC degradation rate but exerts little impact on the final degradation efficiency. Notably, the degradation efficiency remained above 90% across different initial TC concentrations, demonstrating the system's good universality.

$$HSO_5^- + SO_4^{\bullet -} \rightarrow SO_4^{2-} + SO_5^{\bullet -} + H^+ \quad (1)$$

$$HSO_5^- + {}^{\bullet}OH \rightarrow SO_5^{\bullet -} + H_2O \quad (2)$$

In the context of practical wastewater treatment applications, the catalytic system's compatibility with varying pH levels is paramount. The removal of TC by NiFe–N-C/PMS at different pH values is depicted in Fig. 3e. When the pH ranges from 5 to 9, the TC removal efficiency exceeds 90%. At pH 11, the TC removal efficiency showed a slight decrease but remained relatively high. Under strongly acidic conditions (pH = 3), the system's degradation efficiency decreases significantly. This is attributed to the predominant existence of PMS as HSO_5^- in acidic environments, which is relatively stable under high H^+ concentration, thus inhibiting PMS dissociation and activation.[41] Nevertheless, the NiFe–N-C/PMS system still achieves 85.0% TC removal even under such strongly acidic conditions. These findings demonstrate that the NiFe–N-C/PMS system can effectively remove TC over a broad pH range, indicating its adaptability to diverse aqueous environments with varying pH conditions and demonstrating its wide applicability.

Wastewater from domestic sources typically contains substantial quantities of anions and organic matter, which impede the degradation process. To simulate real aqueous environments, inorganic anions (NO_3^-, Cl^-, HCO_3^- and $H_2PO_4^-$) and humic acid (HA) are introduced. As illustrated in Fig. 3f, the NiFe–N-C/PMS system achieved TC degradation efficiency exceeding 90% even in such complex matrices, demonstrating the excellent anti-interference capability of this catalytic system. It has been reported that the coexisting substances (anions and HA) tend to react with free radicals in traditional radical-dominated degradation processes, thereby inhibiting degradation effects and reducing reaction efficiency.[42] Thus, it can be inferred that the active species dominating this degradation process may be non-radicals.

3.3 Identification of ROS in the NiFe–N-C/PMS system

To clarify the dominant ROS in the NiFe–N-C/PMS catalytic system, quenching experiments were carried out by the addition of various quenchers. Methanol is typically employed as a scavenger for $^{\bullet}OH$ ($k = 9.7 \times 10^8\ M^{-1}\ s^{-1}$) and $SO_4^{\bullet -}$ ($k = 3.2 \times 10^6\ M^{-1}\ s^{-1}$). *tert*-Butanol (TBA) and furfuryl alcohol (FFA) were utilized for the capture of $\cdot OH$ ($k = 3.2 \times 10^8\ M^{-1}\ s^{-1}$) and $^1O_2$.[43] As demonstrated in Fig. 4a, a substantial decline in degradation efficiency was observed upon the introduction of these quenchers, verifying the involvement of multiple active species in the catalytic system. Among them, *p*-BQ had the least impact on the degradation process, suggesting that only a small amount of $O_2^{\bullet -}$ was generated during the catalytic reaction. Notably, the addition of TBA and MeOH resulted in comparable degradation inhibition effects (28%), confirming the presence of $\cdot OH$ in the system. Conversely, the addition of FFA caused a significant decline in degradation efficiency, dropping from 93.3% to 48.8%. This observation indicates that the non-radical species $^1O_2$ plays a more significant role than the radical species in the degradation process, which is consistent with previous hypotheses. However, $\cdot OH$ was identified as the primary reactive species during PMS activation when using the N-C matrix alone (Fig. S14). Thus, it can be concluded that the introduction of the NiFe alloy fundamentally alters the PMS activation mechanism.

To further determine the presence of the above active species, validation was carried out by electron paramagnetic resonance (EPR) using 5,5-dimethyl-1-pyrroline *N*-oxide (DMPO) and 2,2,6,6-tetramethylpiperidinooxy (TEMP) as spin trapping agents.[44] For comparison, EPR signals of the NiFe–N-C/PMS system were recorded at 0 min and 30 min. Characteristic signals corresponding to DMPO·OH and DMPO–$SO_4^{\bullet -}$ were observed (Fig. 4b). At 0 min, no distinct signals of DMPO–$\cdot$OH and DMPO–$SO_4^{\bullet -}$ were detected, ruling out the possibility of self-induced dissociation of PMS to generate these radicals. At 30 min, a clear DMPO–$\cdot$OH signal with a peak intensity ratio of 1 : 2 : 2 : 1 emerged indicative of the involvement of $\cdot OH$ radicals during TC degradation. Comparably, signals assignable to DMPO–$SO_4^{\bullet -}$ were much weaker. Unlike $\cdot OH$ and $SO_4^{\bullet -}$, weak TEMP–$^1O_2$ signals were detected at 0 min (Fig. 4c), attributed to the self-decomposition of PMS in aqueous solution. At 30 min,

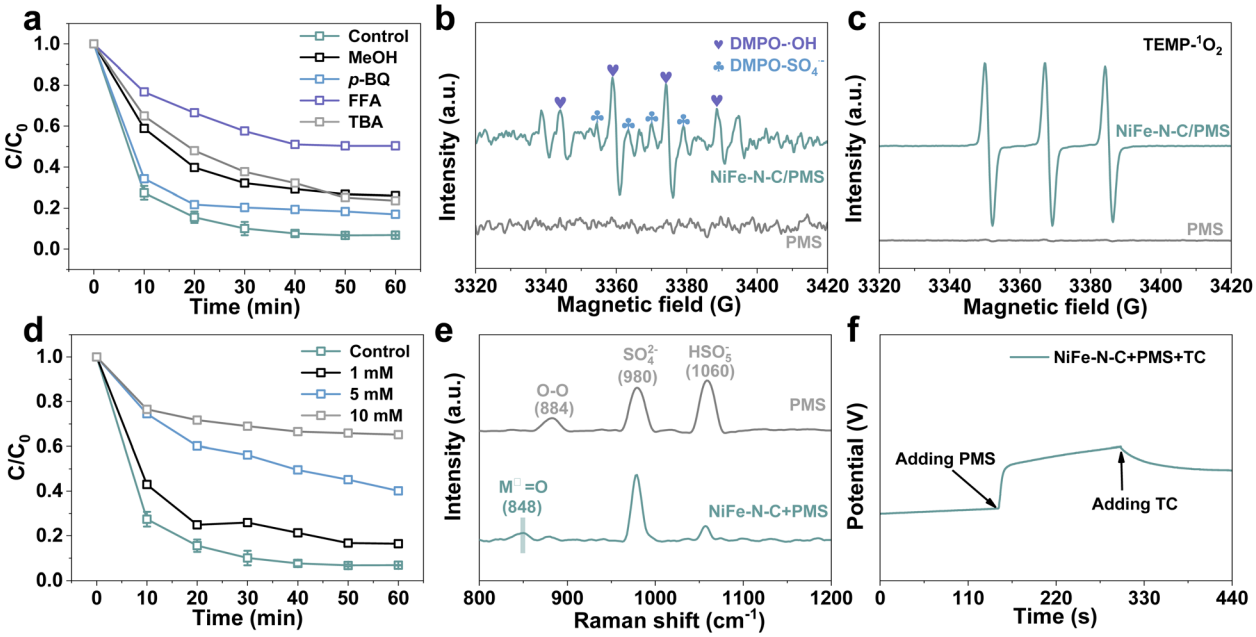

Fig. 4 (a) TC degradation with different kinds of scavengers; EPR spectra of (b) DMPO–·OH and DMPO–$SO_4^{\bullet-}$, and (c) TEMP–$^1O_2$; (d) quenching experiments of the NiFe–N-C/PMS systems by using DMSO; (e) Raman spectra of PMS and NiFe–N-C/PMS systems; (f) open-circuit potential tests.

the TEMP–$^1O_2$ signals were significantly enhanced, reflecting the activation of PMS to generate abundant $^1O_2$. Hence, these EPR results are consistent with the previous findings of the quenching experiments, affirming the presence of the above active species.

It is worth noting that the degradation efficiency remained at approximately 50% after quenching $^1O_2$, confirming the presence of other active species in this catalytic system. Recent studies have confirmed the existence of HVMSs in the metal/PMS system, which enable rapid PMS activation.[44,45] To verify the formation of high-valent $NiFe^{IV}$=O, dimethyl sulfoxide (DMSO) was introduced as a trapping agent into the NiFe–N-C/PMS system. As demonstrated in Fig. 4d, TC removal decreased sharply to 34.8% when the concentration of DMSO increased, directly confirming the generation of $NiFe^{IV}$=O. Subsequently, Raman spectroscopy was conducted to further validate the formation of surface-active species. As illustrated in Fig. 4e, pure PMS exhibited the characteristic peaks at 884 cm^{-1}, 980 cm^{-1}, and 1060 cm^{-1}, assigned to O–O, SO_4^{2-}, and HSO_5^- structures, respectively.[46] Upon the addition of NiFe–N-C, a new characteristic peak emerged at 848 cm^{-1}, which is ascribed to the stretching vibration of the $NiFe^{IV}$=O structure. Additionally, the O–O bond and HSO_5^- peaks markedly weakened, whereas the peak intensity of SO_4^{2-} was significantly enhanced. These observations indicate that PMS induced the formation of HVMSs and concurrently decomposed to generate SO_4^{2-}.[45]

To further elucidate the interaction mechanisms among NiFe–N-C, PMS, and TC, linear scanning voltammetry (LSV) was conducted (Fig. S15). Upon adding PMS, a significant increase in current density was observed, indicating that PMS interacted with the catalyst to induce electron transfer, thereby forming a metastable NiFe–N-C–PMS* complex.[47] When PMS and TC were introduced simultaneously, a further increase in current density was detected. This result confirms that a directional electron flow is established from TC molecules to the NiFe–N-C–PMS* complex, which not only drives the oxidative degradation of TC but also accelerates the redox cycles of the catalyst. Moreover, open-circuit potential (OCP) analysis reveals a significant increase in the potential of NiFe–N-C after PMS addition, whereas a distinct drop in potential was observed following the introduction of TC (Fig. 4f). This charge transfer behaviour originated from the formation and consumption of HVMSs, as $^1O_2$-mediated oxidation reactions predominantly occurred in the solution.[45] Combined with the aforementioned analysis, it can be inferred that the PMS adsorbs on the catalyst surface and forms the metastable NiFe–N-C–PMS* complex *via* electron transfer interactions.[47] This complex undergoes redox reactions to produce ROS (*e.g.*, $^1O_2$), while concurrently driving HVMS formation.

3.4 DFT calculation

Density functional theory (DFT) calculations were conducted with the $FeNi_3$/N-C model to elucidate the formation pathway of high-valent $NiFe^{IV}$=O species and $^1O_2$ in the NiFe–N-C/PMS catalytic system. The projected densities of states (PDOS) corresponding to the spin state of Fe 3d and Ni 3d electrons are shown in Fig. 5a. The d-band center values (ε_d) of Fe 3d and Ni 3d orbitals in $FeNi_3$ were calculated to be −1.311 eV and −1.533 eV, respectively. This result reveals that the d orbital energy level of Fe is closer to the Fermi level than that of Ni, thereby endowing Fe with enhanced adsorption and activation performance toward PMS. Given the isolated distribution of Fe

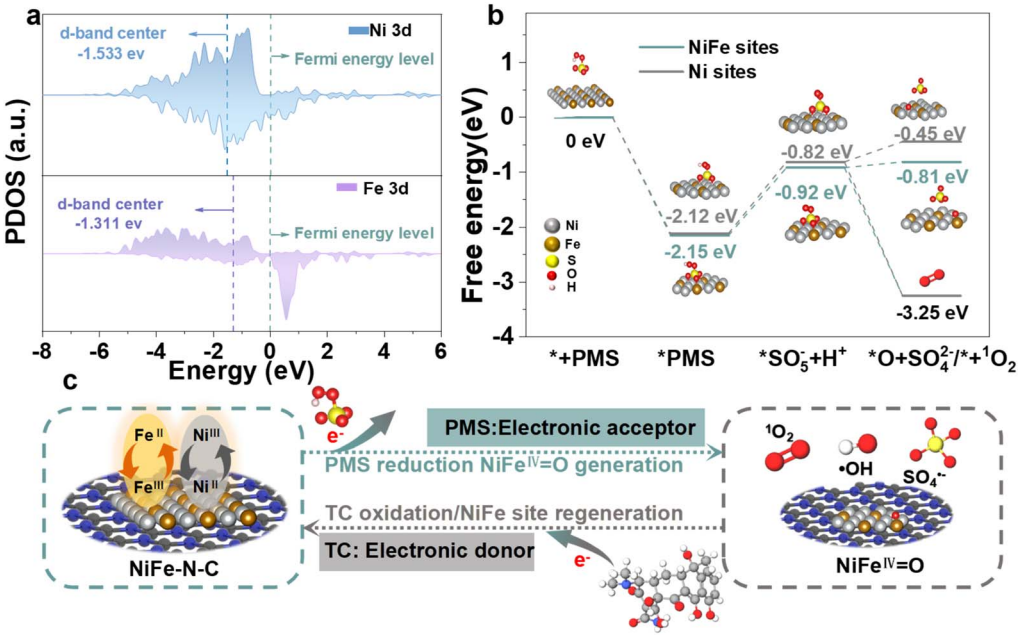

Fig. 5 PDOS of (a) Ni 3d and Fe 3d in NiFe–N-C; (b) the free energy diagrams of PMS activation on Ni/Ni and NiFe sites; (c) proposed mechanism of the NiFe–N-C/PMS system for TC elimination.

species in the $FeNi_3$ crystal, the energy profiles of intermediates during selective PMS activation over Ni/Ni sites and Ni/Fe sites were explored to gain the corresponding thermodynamic mechanistic insights (Fig. 5b). The formation process of HVMSs involves three key steps: initially, PMS molecules are adsorbed onto the catalyst surface and then bind to the metallic active sites through the terminal peroxyl oxygen, resulting in the formation of the catalyst–*PMS complex with free energy changes of −2.15 eV (Ni/Fe sites) and −2.12 eV (Ni/Ni sites), which confirms the strong binding affinity of both Ni/Ni and Fe/Ni active sites toward PMS.[48] Subsequently, a proton transfer process occurs to generate $*SO_5^-$ with the calculated energy differences relative to the initial state being −0.92 eV (Ni/Fe sites) and −0.82 eV (Ni/Ni sites); finally, the O–O bond in the $*SO_5^-$ intermediate undergoes spontaneous radicalization and dissociation, yielding high-valent *O. The energy barrier at Ni/Fe sites is 0.11 eV, much smaller than that at Ni/Ni sites (0.37 eV), indicating that the generation of $NiFe^{IV}$=O is easier than that of Ni^{IV}=O in this process. Notably, the total energy required for $NiFe^{IV}$=O formation (1.34 eV) is lower than that for high-valent Ni^{IV}=O species (1.67 eV). This further demonstrates that Fe and Ni serve as dual active site centers, which synergistically reduce the reaction energy barrier and thus enable the energy-efficient generation of HVMSs. In addition, the $*SO_5^-$ intermediate can spontaneously decompose to produce $^1O_2$ with a free energy of −3.25 eV at both Ni/Ni and NiFe sites, which is highly thermodynamically favorable. Therefore, the overall generation of $^1O_2$ is mainly governed by the energy barrier for $*SO_5^-$ formation and the Ni/Fe dual sites are more conducive to the production of $^1O_2$. The above results fully verify the crucial role of Ni/Fe sites in the generation of both HVMSs and $^1O_2$.

3.5 Proposed reaction mechanisms over the NiFe–N-C/PMS catalytic system

The surface chemical state of NiFe–N-C before and after the reaction was explored by XPS. As seen in Fig. S16a, distinct characteristic peaks of C 1s, N 1s, O 1s, Fe 2p, and Ni 2p were observed in the full survey spectra. For the freshly prepared NiFe–N-C, the Ni 2p spectra (Fig. S16b) can be deconvoluted into six peaks. Peaks at 856.8 eV and 874.5 eV are attributed to Ni^{II} $2p_{3/2}$ and Ni^{II} $2p_{1/2}$, while peaks at 859.6 eV and 877.1 eV correspond to Ni^{III} $2p_{3/2}$ and Ni^{III} $2p_{1/2}$.[49] The peaks at 863.4 eV and 880.4 eV are satellite peaks. After the catalytic reaction, the Ni^{II} content increased from 54.7% to 62.8%, whereas the Ni^{III} content decreased from 45.3% to 37.2%. In the high-resolution Fe 2p spectra (Fig. S16c), the fitted peaks appearing at 709.5 eV and 722.7 eV are Fe^{II} $2p_{3/2}$ and Fe^{II} $2p_{1/2}$. The characteristic peaks at 712.1 eV and 725.7 eV correspond to Fe^{III} $2p_{3/2}$ and Fe^{III} $2p_{1/2}$, with a satellite peak at 716.3 eV.[49] Notably, Fe^{II} decreased slightly from 58.1% to 56.2%, accompanied by a corresponding increase in Fe^{III} from 41.9% to 43.8% after the reactions. Given that $NiFe^{IV}$ exists as a metastable substance, it was not detected in the XPS measurements. Thus, the coexistence of multivalent states of Fe^{II}/Fe^{III} and Ni^{II}/Ni^{III} species, as well as their valence state variations, allows the bimetallic components in NiFe–N-C to engage in dynamic redox cycles, which in turn promote the activation of PMS. Furthermore, the characteristic peaks of Ni^0 and Fe^0 were detected after etching treatment (Fig. S17), confirming that the core of the $FeNi_3$ nanocrystals is indeed retained in the metallic state and serves as electron-donating centers during the catalytic process. Additionally, the N 1s spectra (Fig. S16d) demonstrate that the surface chemical states of nitrogen species remain essentially unchanged after the reaction, indicating that the N-C matrix was stable.

Based on the above analyses, the degradation mechanisms for the NiFe–N-C/PMS system are proposed (Fig. 5c). Firstly, the abundant Fe^{II}/Ni^{II} species on the catalyst surface initiate PMS activation *via* direct interaction. Specifically, Fe^{II}/Ni^{II} species react with HSO_5^- to generate $SO_4^{\cdot-}$ and ·OH, while Fe^{II}/Ni^{II} species are synchronously oxidized to Fe^{III}/Ni^{III} as indicated by eqn (3).[50] Notably, the generated $SO_4^{\cdot-}$ is rapidly converted to ·OH *via* reactions with water (eqn (4)). Furthermore, the *in situ* generated Fe^{III}/Ni^{III} species do not lose activity but continue to interact with HSO_5^- to produce $SO_5^{\cdot-}$. As $SO_5^{\cdot-}$ accumulates in the reaction system, it is ultimately converted to $^1O_2$ through radical recombination or self-decomposition pathways (eqn (6) and (7)), which provide an alternative non-radical route that enhances the system's adaptability to different reaction environments. Notably, Fe^{II} acts as a reducing agent to reduce Ni^{III}, generating Fe^{III} and Ni^{II} in the process (eqn (8)).[51] Notably, the N-C support of the catalyst exhibits excellent electron-donating ability. For Fe^{III}/Ni^{III} adsorbed on the catalyst surface, they can easily acquire electrons from the N-C support. This electron transfer process simultaneously promotes the conversion of Fe^{III}/Ni^{III} to Fe^{II}/Ni^{II} and HSO_5^- to $SO_4^{\cdot-}$ (eqn (9) and (10)). These interconnected reactions collectively establish a stable cyclic regeneration of the Fe^{III}/Fe^{II} and Ni^{III}/Ni^{II} redox pairs, effectively avoiding the accumulation of inactive high-valent

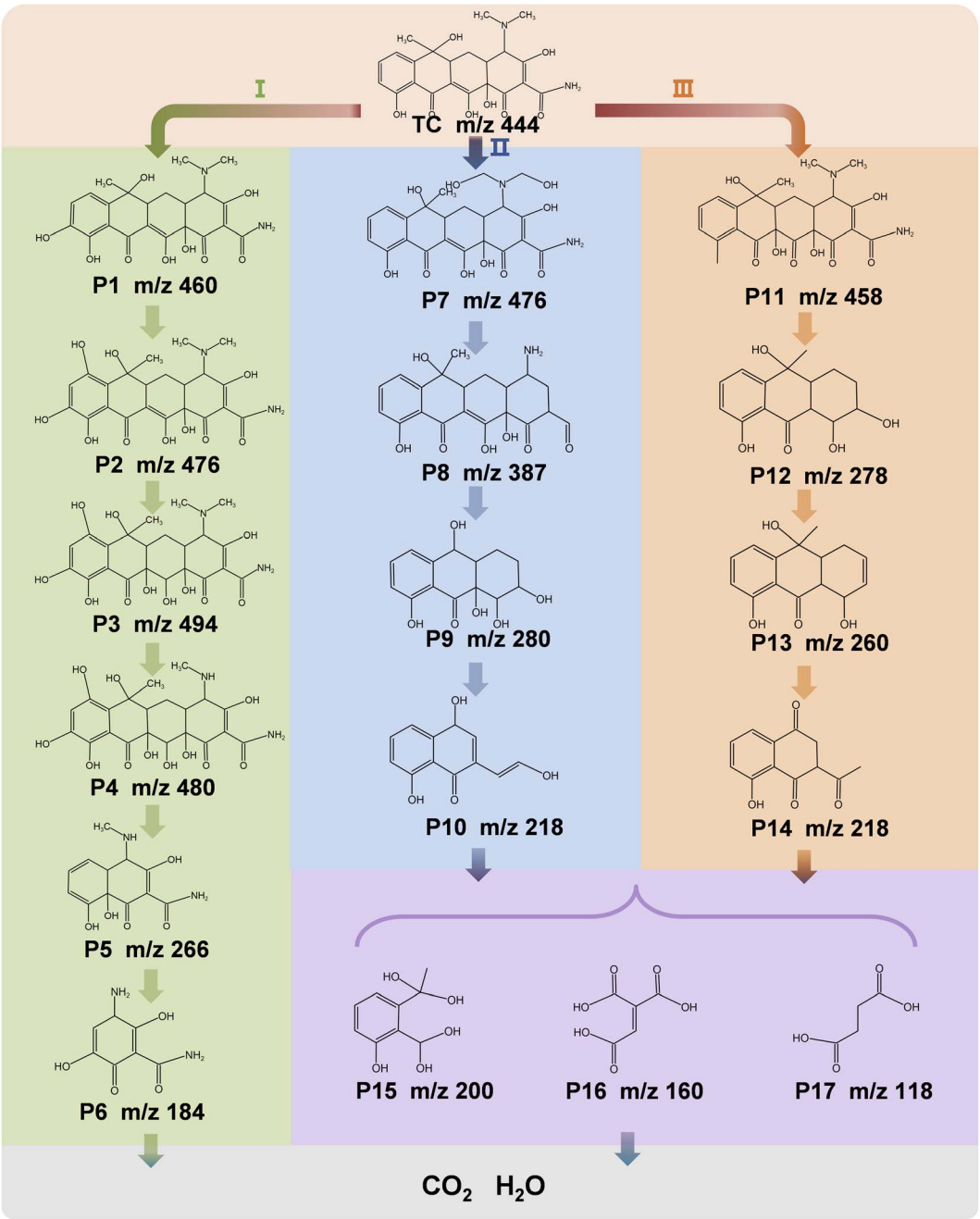

Fig. 6 The potential degradation pathways of TC in the NiFe–N-C/PMS process.

metals and ensuring the long-term PMS activation performance of the catalyst. Besides, Fe^{II}/Ni^{II} can be further oxidized by HSO_5^- to form HVMSs (eqn (11)),[44] which possess extremely strong electrophilic oxidation ability. Finally, the HVMSs and ROS generated through the above reactions synergistically attack the adsorbed TC and decompose it into small molecules.

$$Fe^{II}/Ni^{II} + 2HSO_5^- \rightarrow Fe^{III}/Ni^{III} + SO_4^{\cdot -} + 2^{\cdot}OH + OH^- \quad (3)$$

$$SO_4^{\cdot -} + H_2O \rightarrow SO_4^{2-} + {}^{\cdot}OH + H^+ \quad (4)$$

$$Fe^{III}/Ni^{III} + HSO_5^- \rightarrow Fe^{II}/Ni^{II} + SO_5^{\cdot -} + H^+ \quad (5)$$

$$SO_5^{\cdot -} + SO_5^{\cdot -} \rightarrow S_2O_8^{2-} + {}^1O_2 \quad (6)$$

$$SO_5^{\cdot -} + SO_5^{\cdot -} \rightarrow 2SO_4^{2-} + {}^1O_2 \quad (7)$$

$$Fe^{II} + Ni^{III} \rightarrow Fe^{III} + Ni^{II} \quad (8)$$

$$Fe^{III}/Ni^{III} + e^- \rightarrow Fe^{II}/Ni^{II} \quad (9)$$

$$HSO_5^- + e^- \rightarrow SO_4^{\cdot -} + OH^- \quad (10)$$

$$Fe^{II}/Ni^{II} + HSO_5^- \rightarrow FeNi^{IV}{=}O + SO_4^{2-} + H^+ \quad (11)$$

3.6 Degradation pathways and ecotoxicity assessment

The UV-visible absorption spectra of TC during the degradation process are depicted in Fig. S18. Two characteristic absorption peaks appear at 275 nm and 355 nm, which are assigned to the $\pi \rightarrow \pi^*$ transitions of the conjugated B-ring and $n \rightarrow \pi^*$ transition of the β-diketone moiety (A-ring), respectively.[52] With the extension of degradation time, the absorbance intensities of both characteristic peaks decrease gradually and simultaneously. This synchronous attenuation clearly demonstrates the efficient destruction of the core chromophore structures and the effective degradation of the entire TC molecule. The possible intermediate products during the degradation of TC by NiFe–N-C/PMS were identified by LC-MS. Based on the analysis of the results, three possible degradation pathways were postulated (Fig. 6). In pathway I, TC underwent successive hydroxylation reactions driven by reactive species, leading to the continuous generation of intermediates P1 ($m/z = 460$), P2 ($m/z = 476$) and P3 ($m/z = 494$). Subsequently, the methylamino group of P3 was demethylated to form P4 ($m/z = 480$). P4 further underwent ring opening to yield P5 ($m/z = 266$), which was then converted to P6 ($m/z = 184$) *via* continuous ring cleavage.[53] In pathway II, the methylamino of TC first underwent oxidation to form P7 ($m/z = 476$), which is subsequently dehydroxylated to yield P8 ($m/z = 387$). P8 then proceeded through deamination and ring-opening reactions to further generate P9 ($m/z = 280$) and P10 ($m/z = 218$).[54] In pathway III, the TC underwent hydroxylation and rearrangement to form P11 ($m/z = 458$). The double bond of P11 then broke, triggering ring breakage, cleavage, and amino group loss, which ultimately converted it to P12 ($m/z = 278$). Immediately afterward, addition and dehydration reactions occurred, leading to the formation of P13 ($m/z = 260$). Finally, demethylation, oxidation, and ring-opening reactions took place, generating P14 ($m/z = 218$). Accordingly,

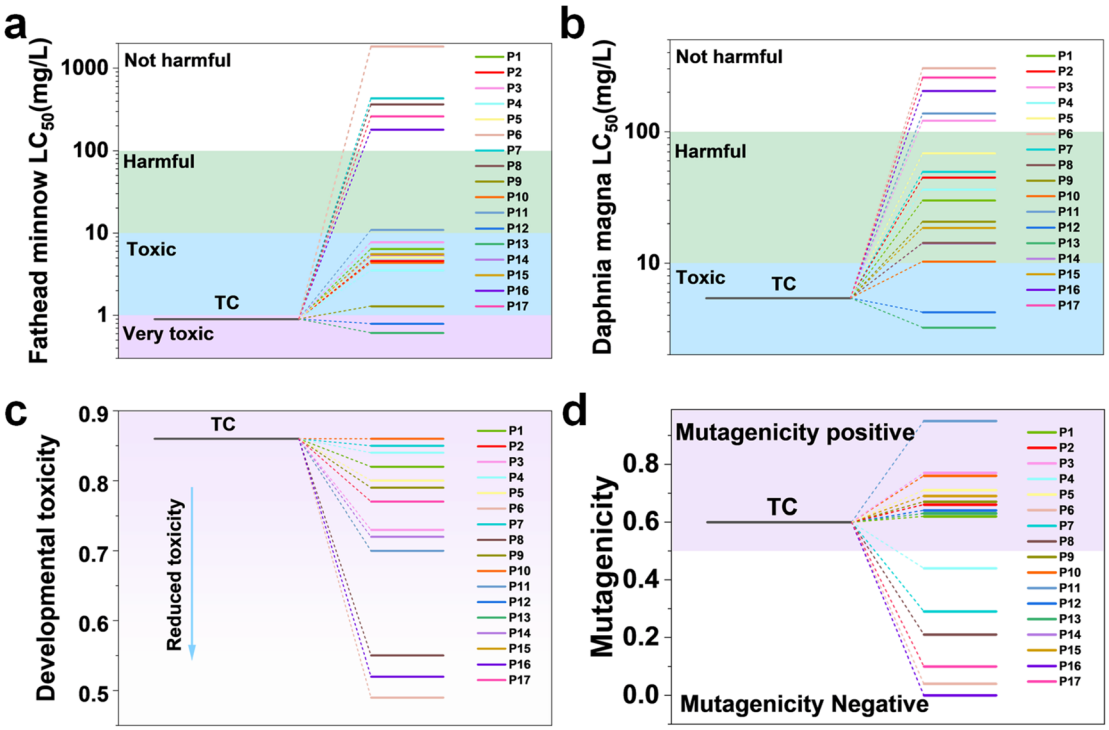

Fig. 7 Toxicity analysis of TC and its degradation intermediates: (a) LC_{50} for fathead minnow; (b) LC_{50} for *Daphnia magna*; (c) developmental toxicity; and (d) mutagenicity.

intermediates P10 and P14 were further oxidized during functional group dissociation and ring opening to form the monocyclic small molecular organics P15 ($m/z = 200$), P16 ($m/z = 160$) and P17 ($m/z = 118$).[54] All these products were eventually mineralized to CO_2, H_2O and other inorganic ions.

Toxicity was assessed using the Toxicity Estimation Software Tool (T.E.S.T) with toxicity classification following the Globally Harmonized System (GHS) of Classification and Labeling of Chemicals.[55] Fig. 7a shows the LC_{50} values obtained for TC and its degradation intermediates in *Fathead minnow* toxicity tests. TC is designated as "very toxic" due to its LC_{50} value of 0.9 mg L^{-1},[56] while all intermediates other than P12 and P13 show higher LC_{50} values, indicating these byproducts are less toxic than TC. Notably, as the degradation process proceeds, P12 and P13 are eventually converted into low toxicity P15 as well as harmless P16 and P17, further confirming the toxicity reduction trend. Fig. 7b presents the LC_{50} values for *Daphnia magna*. For this species, the LC_{50} of TC is 5.44 mg L^{-1}, and consistent with the results for *Fathead minnow*, most intermediates have higher LC_{50} values than TC, further indicating their toxicity is significantly reduced. Fig. 7c provides developmental toxicity. TC has a developmental toxicity value of 0.86, while all degradation intermediates show lower developmental toxicity values than TC. This indicates that the catalytic reaction process can significantly reduce the developmental toxicity of the pollutant. Fig. 7d shows mutagenicity results for TC and its intermediates. TC has a mutagenicity value of 0.60, which was classified as "mutagenicity positive", while the final small-molecule products P6 (0.04), P16 (0), and P17 (0.10) have much lower mutagenicity values than TC, indicating that the catalytic reaction reduces the mutagenicity. These toxicity prediction results confirm that the NiFe–N-C catalyst can effectively activate PMS to remove TC while reducing its overall toxicity throughout the process.

4. Conclusions

In summary, NiFe–N-C catalysts with stabilized skeleton structures were successfully synthesized by high-temperature pyrolysis. Compared to the pristine N-C matrix, NiFe–N-C exhibited significantly enhanced electrochemical activity and accelerated electron transfer kinetics. After optimizing the experimental conditions, the NiFe–N-C/PMS catalytic system achieved 93.3% TC removal and 79.8% PMS utilization within 60 minutes, demonstrating efficient pollutant degradation and oxidant utilization. Notably, this catalytic system displayed minimal susceptibility to common coexisting anions and HA in various aqueous matrices, while retaining excellent catalytic performance over a wide pH range, highlighting its strong environmental adaptability. Quenching experiments and EPR analysis confirmed that HVMSs and $^1O_2$ were the dominant active species. DFT calculation revealed that Ni/Fe dual active sites could reduce the energy barrier for O–O bond cleavage in PMS, thereby facilitating the formation of HVMSs and $^1O_2$. Additionally, the N-C matrix-facilitated rapid Fe^{II}/Fe^{III} and Ni^{II}/Ni^{III} redox cycles preferentially promoted PMS activation. Furthermore, the intermediates produced during TC degradation were identified *via* LC-MS, and the corresponding degradation pathways were proposed, involving sequential steps of hydroxylation, demethylation, deamination, ring opening, and further oxidation. Finally, toxicity analysis confirmed that the toxicity of TC was effectively abated throughout the catalytic process. This study not only provides a comprehensive understanding of the NiFe–N-C/PMS catalytic system but also offers valuable insights for the development of efficient, stable, and environmentally adaptive catalytic technologies for antibiotic degradation in practical water treatment scenarios.

Author contributions

Xiaoqin Sun: conceptualization, methodology, writing – review & editing, and funding acquisition. Meiluo Jiang: investigation, methodology, data curation, formal analysis, and writing – original draft. Hao Chen: software and validation. Hongmei Chen: data curation. Xiaoxiang Xu: methodology, supervision, and writing – review & editing.

Conflicts of interest

There are no conflicts to declare.

Data availability

The data supporting this article have been included as part of the supplementary information (SI). Supplementary information: experimental details, SEM, TGA, BET, TOC removal, activation of various oxidants, stability of the catalyst, optimization of the catalytic system, XPS and activity comparisons. See DOI: https://doi.org/10.1039/d5ta10557a.

Acknowledgements

This study was supported by the Natural Science Foundation of Shaanxi Province (No. 2025JC-YBQN-215), the National Natural Science Foundation of China (Grant No. 52572256), the Tongji University Medicine-X Interdisciplinary Research Initiative (Grant No. 2025-0717-YB-01), and the Startup Fund (No. XM202500001) from the Institute of Wenzhou, Zhejiang University.

References

1 A. S. Oberoi, Y. Jia, H. Zhang, S. K. Khanal and H. Lu, *Environ. Sci. Technol.*, 2019, **53**, 7234–7264.
2 Y. Li, Q. An, Z. Xiao, K. Zhu, X. Zhang, C. Wang, Y. Liu and S. Zhai, *Chem. Eng. J.*, 2024, **487**, 150636.
3 Z. Xie, D. D. Dionysiou, S. Luo, M. Chen and Z. Wei, *Appl. Catal., B*, 2023, **327**, 122468.
4 X. Lan, H. Jiajia, W. Yinsu and X. Shengtao, *Chem. Eng. J.*, 2022, **436**, 135260.
5 C. Wang, Z. Lv, J. Deng, T. Cao, M. Kim, H. Kang, J. Wang, R. Peng, X. Zhu and Y. Mao, *Chem. Eng. J.*, 2024, **498**, 155103.

6 J. Miao, Y. Zhu, J. Lang, J. Zhang, S. Cheng, B. Zhou, L. Zhang, P. J. J. Alvarez and M. Long, *ACS Catal.*, 2021, **11**, 9569–9577.
7 R. Zhao, D. Chen, H. Liu, H. Tian, R. Li and Y. Huang, *J. Hazard. Mater.*, 2024, **476**, 135068.
8 S. Jin, W. Tan, X. Tang, M. Li, X. Yu, H. Zhang, S. Song and T. Zeng, *Small*, 2024, **20**, 2405012.
9 I. B. Baguc, M. Yurderi, A. Bulut, M. Celebi, G. S. Kanberoglu, M. Zahmakiran, M. Kaya, M. Aydemir, F. Durap and A. Baysal, *Int. J. Hydrogen Energy*, 2019, **44**, 28441–28450.
10 Y. Xu, J. Ai and H. Zhang, *J. Hazard. Mater.*, 2016, **309**, 87–96.
11 Y. Li, D. Lin, Y. Li, P. Jiang, X. Fang and B. Yu, *Nano Res.*, 2022, **16**, 155–165.
12 C. Q. Zhu, F. X. Cun, Z. W. Fan, Y. Nie, Q. Du, F. Q. Liu, W. B. Yang and A. M. Li, *Water Res.*, 2023, **241**, 120164.
13 I. C. Gerber and P. Serp, *Chem. Rev.*, 2020, **120**, 1250–1349.
14 H.-J. Niu, L. Zhang, J.-J. Feng, Q.-L. Zhang, H. Huang and A.-J. Wang, *J. Colloid Interface Sci.*, 2019, **552**, 744–751.
15 G. Wang, S. Chen, X. Quan, H. Yu and Y. Zhang, *Carbon*, 2017, **115**, 730–739.
16 T. Xiao, Y. Tao, S. Hou, H. Wang, J.-Q. Xie, Y. Chang, Q. Fu, K. Du and S. Zhou, *Sep. Purif. Technol.*, 2024, **356**, 129916.
17 M. Hu, D. Zhao, X. Yan, Y. Wang, J. Zhang, X. Hu, M. Zhou and P. Liu, *Appl. Catal. B Environ. Energy*, 2024, **362**, 124753.
18 Y. Wang, X. Li, W. Xu, D. Chen, N. Li, Q. Xu, H. Li and J. Lu, *Appl. Catal. B Environ. Energy*, 2024, **348**, 123839.
19 C. Zhang, M. Wang, K. Gao, H. Zhu, J. Ma, X. Fang, X. Wang and Y. Ding, *Small*, 2022, **19**, 2205706.
20 M. Tang and Y. Zhang, *RSC Adv.*, 2021, **11**, 38003–38015.
21 J. Huang, S. Virji, B. H. Weiller and R. B. Kaner, *J. Am. Chem. Soc.*, 2003, **125**, 314–315.
22 K. Gong, F. Du, Z. Xia, M. Durstock and L. Dai, *Science*, 2009, **323**, 760–764.
23 L. Fan, P. F. Liu, X. Yan, L. Gu, Z. Z. Yang, H. G. Yang, S. Qiu and X. Yao, *Nat. Commun.*, 2016, **7**, 10667.
24 C. M. Zhang, M. Wang, K. Y. Gao, H. B. Zhu, J. Ma, X. L. Fang, X. F. Wang and Y. Ding, *Small*, 2023, **19**, 2205706.
25 H. Mao, X. Liu, S. Wu, Y. Fu, G. Liu, G. Zhou and L. Wang, *Nano Res.*, 2022, **16**, 2519–2527.
26 D. Varghese, M. Joe Raja Ruban, P. Joselene Suzan Jennifer, D. AnnieCanisius, S. Chakko, S. Muthupandi, J. Madhavan and M. Victor Antony Raj, *RSC Adv.*, 2023, **13**, 28339–28361.
27 X. Sun, T. Wang and X. Xu, *Int. J. Hydrogen Energy*, 2024, **68**, 149–158.
28 W. Y. Wang, Y. Y. Wang, X. Q. Wang, B. L. Jiang and H. Song, *ACS Appl. Mater. Interfaces*, 2022, **14**, 41912–41923.
29 J. Huang, W. Wang, T. Wu, X. Ren and X. Zhao, *RSC Adv.*, 2024, **14**, 16150–16169.
30 Y. Gao, Z. Chen, Y. Zhu, T. Li and C. Hu, *Environ. Sci. Technol.*, 2020, **54**, 1232–1241.
31 X. Zhou, Y. T. Zhou, S. C. Zhao, S. H. Fan, X. He, J. F. Yu, L. Tang and J. J. Wang, *Adv. Funct. Mater.*, 2025, **12**, e13232.
32 A. E. ElMetwally, F. Goodarzi, K. K. Meier, E. M. Zahran, S. Rayat, S. Kegnæs, M. R. Knecht and L. G. Bachas, *ACS Appl. Nano Mater.*, 2021, **4**, 12222–12234.
33 L. Kong, G. Liu, Y. Liu, B. Cai, S. Zhan and J. Zhan, *Chem. Eng. J.*, 2023, **480**, 148084.
34 S. Wacławek, H. V. Lutze, K. Grübel, V. V. T. Padil, M. Černík and D. D. Dionysiou, *Chem. Eng. J.*, 2017, **330**, 44–62.
35 J. Gu, H. Wang, S. Li, M. Sohail Riaz, J. Ning, X. Pu and Y. Hu, *J. Colloid Interface Sci.*, 2022, **635**, 254–264.
36 J. Han, J. Cho, J.-C. Kim and R. Ryoo, *ACS Catal.*, 2018, **8**, 876–879.
37 Y. Yao, J. Yang, C. Zhu, L. Lu, Q. Fang, C. Xu, Z. He, S. Song and Y. Shen, *J. Hazard. Mater.*, 2024, **462**, 132739.
38 J. Zang, H. Wang, P. You and G. Fan, *Chem. Eng. J.*, 2025, **522**, 167441.
39 J. Zhang, J.-F. Xie, J.-C. E. Yang, D. Li, L.-B. Zhong and Y.-M. Zheng, *Chem. Eng. J.*, 2023, **477**, 146961.
40 T. Liu, K. Cui, Y. Chen, C. Li, M. Cui, H. Yao, Y. Chen and S. Wang, *Chemosphere*, 2021, **283**, 131188.
41 T. Zhang, H. Zhu and J.-P. Croué, *Environ. Sci. Technol.*, 2013, **47**, 2784–2791.
42 G. Wang, Y. Liu, X. Dong and X. Zhang, *J. Hazard. Mater.*, 2022, **437**, 129357.
43 L. Wojnárovits, T. Tóth and E. Takács, *Crit. Rev. Environ. Sci. Technol.*, 2018, **48**, 575–613.
44 Y. He, H. Qin, Z. Wang, H. Wang, Y. Zhu, C. Zhou, Y. Zeng, Y. Li, P. Xu and G. Zeng, *Appl. Catal. B Environ. Energy*, 2023, **340**, 123204.
45 Y. X. Zou, S. H. Fu, Z. Y. Xu, X. C. Zhou, J. Li, Y. Y. Zhang, Y. Lu, S. Y. Li and T. T. Zhang, *Chem. Eng. J.*, 2025, **505**, 159684.
46 Y. C. Li, Z. Y. Feng, H. B. Jia, S. H. Zou, T. Yang, M. F. Li, Y. A. Huang and H. Y. Zhao, *Angew. Chem., Int. Ed.*, 2025, **64**, e202512925.
47 C. Zhao, L. Meng, H. Chu, J.-F. Wang, T. Wang, Y. Ma and C.-C. Wang, *Appl. Catal. B Environ. Energy*, 2022, **321**, 122034.
48 C. Zuo, Q. Su, J. Wang, H. Zhao, M. Wang, X. Tai and X. Wang, *Sci. China Mater.*, 2026, **69**, 249–261.
49 X. Q. Sun, H. H. Xi, Y. Dang and S. N. Yun, *J. Environ. Chem. Eng.*, 2025, **13**, 116300.
50 Y. Liu, J. Gao, Q. Wang, H. Chen, Y. Zhang and X. Fu, *J. Hazard. Mater.*, 2024, **469**, 133869.
51 Z. Yang, k. Yang and C. Zhang, *Sep. Purif. Technol.*, 2023, **333**, 125885.
52 B. Gao, S. Iftekhar, V. Srivastava, B. Doshi and M. Sillanpää, *Catal. Sci. Technol.*, 2018, **8**, 2186–2194.
53 Y. Hu, D. Chen, R. Zhang, Y. Ding, Z. Ren, M. Fu, X. Cao and G. Zeng, *J. Hazard. Mater.*, 2021, **419**, 126495.
54 W. Li, D. Zhou, H. Jiang, H. Chen, J. Guo, J. Yang, X. Wang, H. Wang, X. Yuan and L. Jiang, *Sep. Purif. Technol.*, 2024, **346**, 127509.
55 H. Wang, H. Chen, Q. Wan, Y. Zheng, Y. Wan, X. Liu, X. Song, W. Ma and P. Huo, *Chem. Eng. J.*, 2025, **514**, 163192.
56 R. Chen, H. Zhang, Y. Dong and H. Shi, *J. Mater. Sci. Technol.*, 2024, **170**, 11–24.

